Catalysis Today 182 (2012) 25–38

Contents lists available at SciVerse ScienceDirect

Catalysis Today

journal homepage: www.elsevier.com/locate/cattod

Effects of the crystal reduction state on the interaction of oxygen with rutile $TiO_2(1\,1\,0)$

Estephania Lira[a], Peipei Huo[a], Jonas Ø. Hansen[a], Felix Rieboldt[a], Ralf Bechstein[a], Yinying Wei[a], Regine Streber[a], Soeren Porsgaard[a], Zheshen Li[b], Erik Lægsgaard[a], Stefan Wendt[a,*], Flemming Besenbacher[a]

[a] Interdisciplinary Nanoscience Center (iNANO), Department of Physics and Astronomy, Aarhus University, DK-8000 Aarhus C, Denmark
[b] Institute for Storage Ring Facilities (ISA), Aarhus University, DK-8000 Aarhus C, Denmark

ARTICLE INFO

Article history:
Received 20 June 2011
Received in revised form 8 August 2011
Accepted 20 September 2011
Available online 22 October 2011

Keywords:
TiO_2
Ti^{3+} excess charge
O_2 dissociation
O_2 desorption
Scanning tunneling microscopy (STM)
Temperature-programmed desorption (TPD)

ABSTRACT

The interaction of O_2 with reduced rutile $TiO_2(1\,1\,0)$–(1×1) has been studied by means of scanning tunneling microscopy (STM), temperature-programmed desorption (TPD) and photoelectron spectroscopy (PES). It is found that the interaction of O_2 with $TiO_2(1\,1\,0)$ depends strongly on the reduction state of the $TiO_2(1\,1\,0)$ crystal. High-resolution STM studies revealed that the energy barrier for the non-vacancy-assisted, 2nd O_2 dissociation channel decreases with increasing crystal reduction. Additionally, it is found in the STM studies that the Ti interstitial diffusion is slightly more facile in high-reduced $TiO_2(1\,1\,0)$ crystals compared to low-reduced ones. Accompanying TPD studies revealed that the line shape of the O_2-TPD peak occurring between ~360 K and ~450 K depends on the crystal reduction state. For high-reduced $TiO_2(1\,1\,0)$ crystals characterized by large terraces most O_2 molecules desorb at ~386 K, whereas O_2 desorption is peaking at ~410 K for low- and medium-reduced crystals. Furthermore, the O_2-TPD experiments revealed a highly non-linear behavior of the O_2 desorption peak integrals as function of the crystal reduction state. The presented results point to an ionosorption model where the adsorbates withdraw the excess charge (Ti^{3+}) from the near-surface region at temperatures < ~360 K and where Ti interstitials react with oxygen species on the surface at temperatures ≥ ~360 K.

1. Introduction

Titanium dioxide (TiO_2) is used in a wide number of technological fields such as photocatalysis, heterogeneous catalysis, biocompatible materials, photovoltaic cells and gas sensors [1–9]. In all these applications the interaction of O_2 with TiO_2 plays an important role. For example, O_2 is a common oxidant and is used in photocatalysis as a scavenger of the photoexcited electrons to prevent negative charge accumulation on the surface of the catalysts [1,2,5,9]. Thus, to enhance the efficiencies in the current and future applications of TiO_2 it is essential to improve our fundamental understanding of how O_2 interacts with TiO_2 surfaces.

It is generally accepted that adsorbed O_2 species acquire negative charge upon adsorption on TiO_2 surfaces [7,9–18]. Theoretical calculations have shown that excess charge can be donated by all the various defects that are associated with Ti^{3+} such as O vacancies, surplus H and interstitial Ti [12,14,15,18–24]. The Ti^{3+} excess electrons populate the normally empty Ti 3d orbitals on cations in the near and far proximity of the structural defects, leading to a state in the ~3.1 eV wide band gap [4,10,13,25–29]. It is this excess charge that can be donated to O_2 species on the TiO_2 surface [4,7,9–13,15–18,26,27,30,31]. However, which particular structural defects provide most of the Ti^{3+} excess electrons and are thus most relevant for the O_2–TiO_2 interaction is today still unsettled [9,17,30,32].

To disentangle the contributions of the individual defects for chemical reactions on TiO_2, the surface science approach [33] is most promising. For surface science studies addressing TiO_2, the rutile $TiO_2(1\,1\,0)$–(1×1) surface has been often preferred (Fig. 1) [4,7,17,32,34,35]. Upon $TiO_2(1\,1\,0)$ sample preparation in ultrahigh vacuum (UHV), the crystals are reduced, leading to the creation of bulk defects such as Ti interstitials and bridging O (O_{br}) vacancies on the surface [4,13,35,36]. Considering that scanning tunneling microscopy (STM) studies addressing the anatase $TiO_2(101)$ surface revealed the absence of surface O vacancies [37], the formation of surface O vacancies in UHV may be a peculiar feature of rutile crystals.

The interaction of O_2 with rutile $TiO_2(1\,1\,0)$ has been studied previously using STM [4,13,17,30,32,35,38–49], temperature

* Corresponding author at: Ny Munkegade, Bldg. 1522, Office 1522-130, DK-8000 Aarhus C, Denmark. Tel.: +45 8942 5538; fax: +45 8612 0740.
E-mail address: swendt@phys.au.dk (S. Wendt).

0920-5861/$ – see front matter © 2011 Elsevier B.V. All rights reserved.
doi:10.1016/j.cattod.2011.09.038

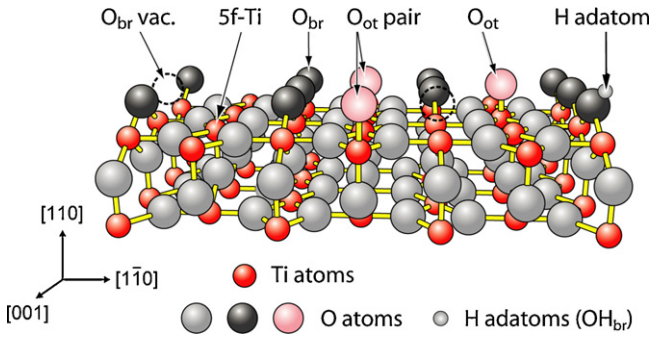

Fig. 1. (a) Ball-and-stick model of the rutile $TiO_2(1\,1\,0)$–(1×1) surface with O_{br} vacancies, H adatoms (OH_{br}), and single as well as paired O_{ot} adatoms. Large dark gray balls represent twofold coordinated O_{br} atoms, large light gray balls threefold coordinated O atoms and large pink balls O_{ot} adatoms. Small red balls represent Ti atoms and light gray balls H adatoms. (For interpretation of the references to color in this figure legend, the reader is referred to the web version of this article.)

programmed desorption (TPD) [10,11,30,49–52], photoelectron spectroscopy (PES) [13,25–27,53] and photon- or electron-stimulated desorption (PSD, ESD) [7,11,16,31,45,52,54–59]. At low temperatures (LT), that is for $110\,K \leq T \leq 150\,K$, O_2 molecules adsorb both molecularly and dissociatively on rutile $TiO_2(1\,1\,0)$ [13,30,41,45], whereas at room temperature (RT) dissociative adsorption is prevalent in low-pressure-experiments performed under UHV conditions [10,13,30,44]. Two different dissociative adsorption channels have been identified at RT: The 1st channel that is associated with O_{br} vacancy sites and the 2nd channel that occurs directly in the Ti troughs and is not associated with O_{br} vacancy sites [13,30,44]. As a result of dissociative O_2 adsorption, O adatoms are created that reside on-top on the 5f-Ti sites (O_{ot} adatoms, cf. Fig. 1). In the STM images, the O_{ot} adatoms appear as bright protrusions in the Ti troughs, rendering STM as the technique of choice for studying the dissociative adsorption of O_2 on $TiO_2(1\,1\,0)$.

Recent low-temperature STM studies [46–48] confirmed the occurrence of molecular and dissociative adsorption of O_2, and also the existence of two O_2 dissociation channels has been confirmed by Wang et al. [47]. However, uncertainty still exists with regard to the temperatures at which the two O_2 dissociation channels set in. Whereas we found the onset of the 1st O_2 dissociation channel to occur at 110–130 K [13,41], Tan et al. [48] reported evidence for nondissociated O_2 at O_{br} vacancies at 130 K, and Wang et al. [47] reported that O_2 molecules would dissociate only for temperatures higher than 150 K.

Regarding the role of defects for the interaction of O_2 with rutile $TiO_2(1\,1\,0)$, Petrik et al. claimed that the amount of chemisorbed O_2 on TiO_2 depends mainly on the density of surface defects such as O_{br} vacancies and capping H adatoms [H_{ad} species, also known as bridging hydroxyl (OH_{br}) groups] [31]. These authors inferred that the Ti^{3+} excess charge associated with O_{br} vacancies and H_{ad} species rather than the charge provided from subsurface defects, such as Ti interstitials, determines the oxygen chemistry on rutile $TiO_2(1\,1\,0)$–(1×1) [31]. The same group also suggested that the excess charge associated with the 2nd, non-vacancy-assisted O_2 dissociation channel would stem predominantly from O_{br} vacancies [44] rather than from Ti interstitials as we proposed earlier [13]. Recently, we have provided further evidence that the adsorption of oxygen species on clean, reduced $TiO_2(1\,1\,0)$ surfaces is governed by the available Ti^{3+} excess charge in the near-surface region [30,49]. Specifically, we proposed that the desorption of O_2 molecules at ~410 K is caused by a depletion of Ti^{3+} excess charge in the near-surface region induced by reactions between oxygen species and out-diffusing Ti interstitials [30]. These observations point to an ionosorption model for understanding redox processes on the surface of reduced $TiO_2(1\,1\,0)$ rather than to charge donation from surface defects.

In the present article, we studied the interaction of O_2 with reduced $TiO_2(1\,1\,0)$–(1×1) surfaces for a wide range of crystal reduction states. We report on a strong influence of the crystal reduction state on the O_2 adsorption. An upper limit exists for the coverage of O_{ot} adatoms that can be adsorbed on $TiO_2(1\,1\,0)$. On high-reduced $TiO_2(1\,1\,0)$–(1×1) surfaces this limit lays close to ~8% ML (LT) and ~11% ML (RT), respectively. In addition, the barrier for the 2nd O_2 dissociation channel is lower on high-reduced $TiO_2(1\,1\,0)$ crystals than on low- and medium-reduced ones. Likewise the line shape of the O_2-TPD-spectra depends on the crystal reduction state, and the O_2 desorption peak integrals show a highly non-linear dependence of the crystal reduction state. The presented results can be best explained within an ionosorption model: The adsorbates, O_2 molecules and O_{ot} adatoms, respectively, withdraw the Ti^{3+} excess charge from the near-surface region at <~360 K, and at temperatures ≥ ~360 K the oxygen species react with out-diffusing Ti interstitials.

2. Experimental

The STM and TPD experiments were performed in a UHV chamber with a base pressure in the low 10^{-11} Torr range equipped with a homebuilt, variable-temperature Aarhus STM, a quadrupole mass spectrometer (QMS), and standard facilities for sample preparation and characterization [60,61]. The Aarhus STM is capable of fast scanning and high resolution in a temperature range between 100 and 400 K [60]. Electrochemically etched tungsten tips were used for all STM measurements. The STM images presented in this study were acquired in constant current mode with a tunneling voltage of ~+1.25 V and a tunneling current of ~0.1 nA. Lower tunneling voltages and currents were also tested, and the results were found to be invariant in the covered parameter intervals. For the extraction of coverage based on the STM measurements at least total areas of 1300–2000 nm^2 were scanned and analyzed. From previous studies we know that the analysis of STM images covering ~1000 nm^2 are sufficient in order to guarantee that the observed densities are representative for the whole sample surface [30,42,62].

The differentially pumped QMS was connected to the main chamber via a closed cone with a small aperture ($d \sim 3$ mm). To ensure that only molecules desorbing from the sample could reach the QMS, the cone was placed facing the sample at a distance of ~1 mm. The temperature of the sample could be varied from 100 K by cooling with liquid nitrogen to 1100 K by heating the back side of the sample radiatively and by electron bombardment. The sample temperature was measured using a K-type thermocouple spot-welded to the sample plate such that the thermocouple is in direct contact with the crystal face. The sample temperature was controlled and recorded by a Eurotherm temperature controller that contains an automatic compensation of ambient temperature changes. A calibrated pyrometer was used to double check the temperature of the samples during vacuum-annealing.

The PES experiments were carried out in an UHV end-station at the SX700 plane grating monochromator beam line at the ASTRID synchrotron radiation facility at Aarhus University [63]. The base pressure in this UHV chamber was likewise in the 10^{-11} Torr range. The PES data were acquired using a VG CLAM II spectrometer working at 30 eV pass energy. Valence band spectra were acquired with a photon energy of 47.5 eV, corresponding to the Ti 3p–3d resonance in order to maximize the intensity of the Ti 3d defect state in the band gap [26,64]. All PES spectra were acquired in normal emission geometry and normalized to the incident photon-flux. Spectra are plotted versus binding energy (BE) with respect to the Fermi level, E_F.

To obtain clean TiO_2(1 1 0) surfaces [*r*-TiO_2(1 1 0)], the crystals were several times Ar^+ sputtered (1 keV) at RT and vacuum-annealed at 810–980 K. After vacuum annealing, the samples were flash-annealed at ~600 K for 120 s in order to free the sample from H_{ad} species that result from water adsorption and dissociation during the slow cooling of the sample after the 20 min anneal [41].

If not stated otherwise, clean *r*-TiO_2(1 1 0) surfaces were exposed to O_2 through a directional doser containing a 10 μm glass capillary array disk of ~8 mm diameter, which was placed in front of the sample at a distance of ~1 mm from the sample surface. When using the directional doser, the local O_2 pressure was estimated to be ~100 times higher than the background O_2 pressure. The given O_2 exposures in L (Langmuir), with $1\,L = 1.33 \times 10^{-6}$ mbar s, take this factor of 100 into account. The use of the directional doser is advantageous to minimize the partial O_2 pressure in the UHV chamber and thus to avoid unwanted exchange reactions at the chamber walls that often lead to water contamination of the TiO_2(1 1 0) surface.

To prepare hydrated TiO_2(1 1 0) surfaces [*h*-TiO_2(1 1 0)], deionized water cleaned via freeze-pump-thaw cycles was introduced into the UHV chamber through a leak valve. A short flash to 373 K was applied to promote the diffusion and desorption of excess water molecules. All the densities of adsorbates or defects are given in % ML, with 1 ML being the density of the (1×1) unit cells, $5.2 \times 10^{14}/cm^2$.

3. Results and discussions

3.1. Comparison of r- and h-TiO_2(1 1 0) surfaces

Fig. 2a shows an STM image of a clean, reduced TiO_2(1 1 0) surface [*r*-TiO_2(1 1 0)] that was acquired after 40 cycles of sputtering and annealing. It is well-established that the rows imaged brightly correspond to the five-fold coordinated Ti atoms, the Ti troughs, while the dark rows arise from the protruding two-fold coordinated O_{br} atoms (Fig. 1) [4,65]. Protrusions within the dark rows are known to stem from O_{br} vacancies, i.e., missing O_{br} atoms [4,17,32,34,41]. In addition to the O_{br} vacancies few capping H_{ad} species in the rows of O_{br} atoms are also evident on the surface. The H_{ad} species are the result of water dissociation at O_{br} vacancy sites and appear slightly brighter in the STM images than the O_{br} vacancies [17,34,41,66,67]. Fig. 2c shows a PES valence band spectrum of the *r*-TiO_2(1 1 0) surface that was acquired after applying a comparable preparation protocol (red curve). The valence band of rutile TiO_2(1 1 0) is characterized by bands between ~3 and ~9.5 eV BE that are to a large extent associated with O 2p derived states [25,26,68]. In addition, a state within the band gap is observed at ~0.85 eV below E_F that is associated with Ti 3d excess electrons (Ti^{3+}) and that can be eliminated by O_2 exposure [4,13,25–27]. Fig. 2d shows an O_2-TPD spectrum obtained after the *r*-TiO_2(1 1 0) surface imaged in Fig. 2a was exposed to 100 L O_2 at ~130 K. The maximum O_2 desorption occurred at ~410 K (β-peak) regardless of the O_2 exposure, indicating first-order desorption kinetics. A shoulder at ~386 K (α-peak) was evident in all the O_2-TPD spectra collected from this TiO_2(1 1 0) crystal. Such a double peak structure of the O_2 desorption has also been reported in previous studies [10,30,69].

The same techniques were applied to study *h*-TiO_2(1 1 0) surfaces prepared when using crystals characterized by very similar reduction states (cf. Fig. 2). The *h*-TiO_2(1 1 0) surfaces are characterized by the presence of H_{ad} species (indicated by hexagons in Fig. 2a and b) and the complete absence of O_{br} vacancies [41–43]. The PES valence band spectrum of the *h*-TiO_2(1 1 0) surface (Fig. 2c, blue curve) is very similar to the one obtained for *r*-TiO_2(1 1 0), the only apparent difference being a peak found at ~10.3 eV arising from OH 3σ bonds [26]. Upon hydration, the Ti 3d defect state at ~0.85 eV BE remains almost unchanged [13]. The O_2-TPD spectrum obtained for *h*-TiO_2(1 1 0) after O_2 saturation at ~130 K is characterized by a narrow peak that is centered at ~410 K [Fig. 2d, blue curve]. Its integrated area is comparable to that found on the *r*-TiO_2(1 1 0) surface [31,49,50].

The results summarized in Fig. 2 reveal that the electronic properties of *r*- and *h*-TiO_2(1 1 0) surfaces are similar. Consequently, the ability to chemisorb oxygen species is also similar on *r*- and *h*-TiO_2(1 1 0) surfaces. The different line shape of the O_2-TPD spectra found for *r*- and *h*-TiO_2(1 1 0) surfaces may be linked to the different distribution of the Ti^{3+} excess charge in the near-surface region of these crystals. Filled-state STM images published by Minato et al. [29] suggest that the polaronic distortions on *h*-TiO_2(1 1 0) are smaller than that on *r*-TiO_2(1 1 0) surfaces. Taking additionally into account that the density of H_{ad} species on *h*-TiO_2(1 1 0) is about twice as high as the density of O_{br} vacancies on the corresponding *r*-TiO_2(1 1 0) surface, it is very likely that the Ti^{3+} excess charge on *h*-TiO_2(1 1 0) surfaces is distributed much more homogeneously than on *r*-TiO_2(1 1 0) surfaces. An additional factor that may be of relevance when discussing the line shape of the O_2-TPD spectra is the high mobility of H_{ad} species on *h*-TiO_2(1 1 0) surfaces [17]. Because of the high mobility of the H_{ad} species on the surface, a homogeneous distribution of the excess charge can be maintained on *h*-TiO_2(1 1 0), even when the temperature of the crystal is increased within a TPD experiment. On the contrary, upon heating of O_2 exposed *r*-TiO_2(1 1 0) surfaces, the Ti^{3+} excess charge is expected to be distributed rather inhomogeneously because highly mobile charge carriers that are able to diffuse across the surface do not exist on *r*-TiO_2(1 1 0). Note that the desorption of O_2 molecules between ~360 K and at ~450 K can be best understood by considering the available excess charge in the near-surface region: O_2 molecules desorb from the crystal surface when Ti^{3+} excess charge is lacking [30]. Because Ti interstitials diffuse towards the surface upon heating of O_2-exposed *r*-TiO_2(1 1 0) surfaces where they react with the oxygen species, the Ti^{3+} excess charge is depleted in the near-surface region [30,45]. Upon formation of TiO_x islands on the terraces, the Ti^{3+} excess charge depletes because the main charge donors – the Ti interstitials – are consumed, and refilling of interstitials sites in the near-surface region through diffusion of Ti interstitial from deeper layers begins only when the sample has reached temperatures higher than 400 K [13].

3.2. Appearance of O_{ot} adatoms in the STM images

Fig. 3 shows two examples of oxidized TiO_2(1 1 0) surfaces that were prepared in different ways. Whereas the STM image displayed in Fig. 3a was obtained after 25 L O_2 at 140 K, the STM image displayed in Fig. 3b was acquired after oxidation at RT. In both oxidation experiments, new protrusions have appeared in the Ti troughs that arise from O_{ot} adatoms [13,17,30,32,34,41,44,46,48]. Whereas isolated O_{ot} adatoms are prevailing after O_2 exposure at LT, some of the O_{ot} adatoms occur in pairs on next-nearest 5f-Ti sites [*p*(2)-O_{ot} pairs] after O_2 exposure at RT. To clearly distinguish between the different preparations we will in the following designate TiO_2(1 1 0) surfaces prepared by O_2 exposure at LT (110–150 K) as *o*-TiO_2(1 1 0).

On *o*-TiO_2(1 1 0) surfaces, the O_{ot} adatoms are created exclusively via dissociation of O_2 molecules at O_{br} vacancies, i.e., the 1st O_2 dissociation channel [41,46–48]. Because the diffusion of O_{ot} adatoms along the Ti troughs is kinetically hindered at LT [17,41], a one-to-one correlation is expected between the O_{br} vacancies before and the O_{ad} adatoms after the O_2 exposure. For low-reduced TiO_2(1 1 0) crystals this expectation is indeed fulfilled [30]. In contrast, when exposing *r*-TiO_2(1 1 0) surfaces to O_2 at RT, the 2nd O_2 dissociation channel is in play as well, leading to the occurrence

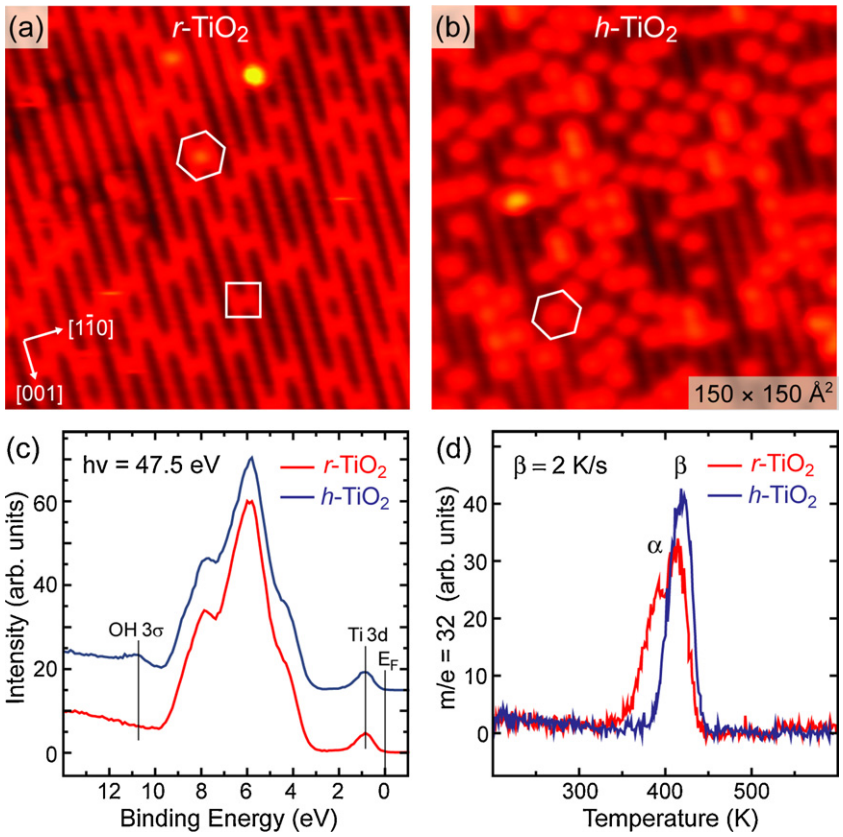

Fig. 2. (a) STM image of a clean r-TiO_2 surface with an O_{br} vacancy density of ~8% ML. The square indicates an O_{br} vacancy and the hexagon an H adatom. (b) STM image of an h-TiO_2 surface obtained after exposing the r-TiO_2 surface to water, followed by flashing to 400 K. (c) Corresponding photoelectron valence band spectra: r-TiO_2 (red) and h-TiO_2 surface (blue), respectively. Spectra are offset for clarity. (d) O_2-TPD spectra obtained after 100 L O_2 exposure at 130 K on r-TiO_2 (red) and h-TiO_2 (blue), respectively. (For interpretation of the references to color in this figure legend, the reader is referred to the web version of this article.)

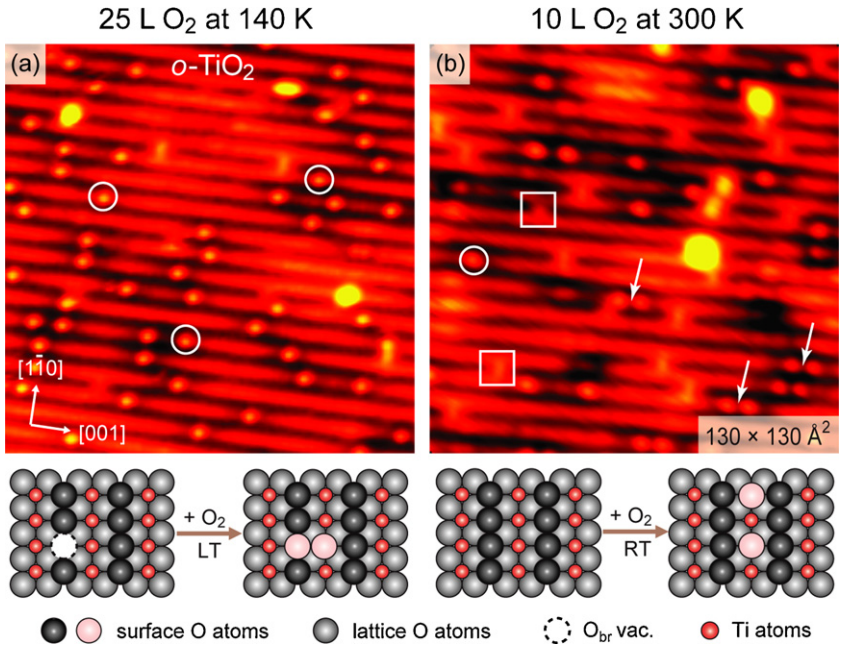

Fig. 3. (a) STM image obtained after 25 L O_2 exposure at 140 K onto medium-reduced TiO_2(1 1 0) with an O_{br} vacancy density of ~7.5% ML. (b) STM image obtained after 10 L O_2 exposure at 300 K onto medium-reduced TiO_2(1 1 0). O_{ot} adatoms are indicated by white circles and p(2)-O_{ot} pairs by white arrows. Squares indicate residual O_{br} vacancies. Schematic models of the two O_2 dissociation channels are shown beneath the STM images.

of $p(2)$-O_{ot} pairs [13,30,44]. In this case, a one-to-one correlation between the O_{br} vacancies before and the O_{ad} adatoms after the O_2 exposure cannot be expected and, indeed, the observed densities of O_{br} vacancies before and the O_{ad} adatoms after the O_2 exposure are different (see below).

Fig. 4 displays zoom-in STM images of O_{ot} adatom pairs together with line profiles through two O_{ot} adatoms in the Ti troughs that are separated by one to four lattice distances. An example of an $p(2)$-O_{ot} pair is shown in Fig. 4a, I together with another pair wherein the O_{ot} adatoms are separated by three lattice distances, Fig. 4a, II. Further examples of O_{ot} adatom pairs are presented in Fig. 4b and c, III and IV, respectively, where two consecutive STM images are depicted. The consecutive STM images were acquired at ~110 K, but the O_2 exposure was accomplished at RT in this experiment. In addition to the $p(2)$-O_{ot} pair seen in Fig. 4a, I the STM images in Fig. 4b and c show nearest-neighbor O_{ot} adatom pairs [$p(1)$-O_{ot} pairs] that appear in the STM images as dumbbell-shaped protrusions and that are indicated by white arrows. Both the $p(1)$-O_{ot} pairs and the $p(2)$-O_{ot} pairs are the product of the 2nd O_2 dissociation channel that is not associated with O_{br} vacancies (see below and Refs. [13,30,44,45,47]). For direct comparison, an isolated O_{ot} adatom is also seen in Fig. 4b and c, cf. the stars.

Line profiles in the [0 0 1] direction taken from the STM image shown in Fig. 4a are displayed in Fig. 4d, while line profiles taken from Fig. 4b and c are displayed in Fig. 4e. As indicated by dotted lines in the STM images, all the line profiles were taken along the Ti troughs and labeled using Roman numbers, I–IV. From the examples shown in Fig. 4 it is clear that the O_{ot} adatoms separated by three lattice spaces [$p(3)$-O_{ot} pairs, II] show up brighter in the STM images than O_{ot} adatoms in $p(2)$-O_{ot} pairs (I). Likewise, the line profiles displayed in Fig. 4d show that O_{ot} adatoms in $p(1)$-O_{ot} pairs (III) appear with much lower heights in the STM images than those occurring in $p(2)$-O_{ot} pairs (IV). Note that the apparent STM height of an isolated O_{ot} adatom (four lattice distances to the closest O_{ot} adatom) is about twice that of the O_{ot} adatoms in the $p(2)$-O_{ot} pairs (Fig. 4e). Clearly, if another O_{ot} adatom is adsorbed close by in the same Ti trough an O_{ot} adatom appears less intense in the STM images than an isolated O_{ot} adatom.

Comparing the consecutive STM images displayed in Fig. 4b and c, respectively, it is seen that the O_{ot} adatom on the right-hand side of pair III has diffused one lattice distance away from the O_{ot} adatom on the left. Consequently, pair IV in Fig. 4c appears as $p(2)$-O_{ot} pair. When scanning on this surface at low temperature (~110 K), we only rarely observed the diffusion of O_{ot} adatoms. Therefore, we believe that the Coulomb repulsion between nearest-neighbor O_{ot} adatoms in the $p(1)$-O_{ot} pair as well as the interaction between the STM tip and the surface has induced the diffusion of this O_{ot} adatom.

According to a Bader charge analysis reported in [13], an isolated O_{ot} adatom withdraws ~0.8 e^- from the TiO_2(1 1 0) substrate. However, when the O_{ot} adatoms occur in pairs, less charge is withdrawn per O_{ot} adatom from the substrate, because excess charge is scarce on the TiO_2(1 1 0) surface. This may explain why the O_{ot} adatoms appear less intense in the STM images if another O_{ot} adatom is adsorbed close by. Nevertheless, the results summarized in Fig. 4 further underline the now well-established fact that the STM images obtained on rutile TiO_2(1 1 0) are strongly influenced by electronic effects [4,65].

Fig. 5 shows further examples of *o*-TiO_2(1 1 0) surfaces with $p(1)$-O_{ot} pairs (white ovals). The STM image depicted in Fig. 5a was acquired on a TiO_2(1 1 0) crystal (O_{br} vacancy density ~9% ML) that was exposed to 6 L O_2 at ~120 K and subsequently heated up to ~266 K. Following this preparation recipe, $p(1)$-O_{ot} pairs appeared on the surface. This result confirms that O_2 molecules are stabilized on the *o*-TiO_2(1 1 0) surface and that the 2nd channel is a thermally activated process [30]. We add that the adjacent O_{ot} adatoms in the STM image depicted in Fig. 5a are very well resolved, which is caused by a special state of the tip apex; most likely, the STM tip had picked up an O or H atom from the surface, which led to the increase in resolution. For a direct comparison between STM images acquired with a special and with a normal tip apex we present in Fig. 5b and c two examples from the same original data file from which the STM image in Fig. 5a was selected, both showing protrusions originating from $p(1)$-O_{ot} pairs. We can easily distinguish whether we are scanning with a bare tungsten tip or with a special tip apex, because the tip changes that occur while scanning are obvious.

3.3. Effect of the reduction state on the dissociative adsorption of O_2 at low temperatures

The STM data summarized in Fig. 6 illustrate the influence of the crystal reduction state on the dissociation of O_2 on *r*-TiO_2(1 1 0) surfaces at LT (110–150 K). In the STM studies, the O_{br} vacancy density was used as a measure of the bulk reduction state. The TiO_2(1 1 0) crystals are classified as low-, medium- and high-reduced for O_{br} vacancy densities of 2–6% ML, 6–9% ML, and 9–12% ML, respectively. In the experiments corresponding to Fig. 6a–c we started with *r*-TiO_2(1 1 0) surfaces characterized by O_{br} vacancy densities of ~4.3% ML, ~7.9% ML, and ~10.6% ML, respectively.

Following O_2 exposure at LT, O_{ot} adatoms were found on all three surfaces, as expected. However, the density of O_{ot} adatoms was only comparable with the density of O_{br} vacancies when the crystal was in a low-reduced state (cf. Fig. 6e). For medium- and high-reduced TiO_2(1 1 0) crystals the O_{ot} densities are smaller than the corresponding O_{br} vacancy densities. Specifically, for the medium-reduced TiO_2(1 1 0) crystal corresponding to Fig. 6b we found 0.7 ± 0.2% ML O_{br} vacancies unfilled, whereas for the high-reduced TiO_2(1 1 0) crystal corresponding to Fig. 6c even 1.8 ± 0.3% ML remain unfilled (cf. Fig. 6e). This indicates that some of the O_{br} vacancies persisted the oxidation on medium- and high-reduced TiO_2(1 1 0) crystals. In addition, we found after oxidation of the high-reduced TiO_2(1 1 0) crystal at 120 K that some of the O_{ot} adatoms appear in $p(1)$-O_{ot} pairs (cf. the hatched area in the bar graph corresponding to Fig. 6c). Note that $p(1)$-O_{ot} pairs have been observed previously only after oxidation at significantly higher temperatures [30]. Our statistical analysis presented in Ref. [30] revealed that the $p(1)$-O_{ot} and $p(2)$-O_{ot} pairs obtained after O_2 exposure at temperatures higher than 150–180 K are the product of O_2 dissociation in the Ti troughs, because the total density of O_{ot} adatoms on the surface has been found to be higher than the O_{br} vacancy densities before the oxidation. In contrast, in the STM experiment corresponding to Fig. 6c and d we are facing a different situation. In this experiment the densities of O_{ot} adatoms and O_{br} vacancies together are smaller than the O_{br} vacancy density before the O_2 exposure.

We have checked whether the $p(1)$-O_{ot} pairs found on the high-reduced TiO_2(1 1 0) crystal are the product of O_2 dissociation events of separate O_2 molecules at nearby O_{br} vacancies (1st O_2 dissociation channel), or whether O_2 molecules dissociate directly in the Ti troughs (2nd O_2 dissociation channel) [70]. At LT, dissociation of O_2 molecules at O_{br} vacancy sites lead preferentially to O_{ot} adatoms at a Ti sites right next to the vacancies [41,46,47]. The probability that two O_{ot} adatoms are created in nearest-neighbor sites can be deduced from the initial distribution of O_{br} vacancies and by considering the starting configurations that can lead to the formation of $p(1)$-O_{ot} pairs (cf. Fig. 7). Configuration A consists of two adjacent O_{br} vacancies in the same row, while configuration B consists of two O_{br} vacancies in adjacent positions in adjacent rows. Assuming that all the dissociation events are independent, each of the four possible pathways of O_{ot} adatom pair formation has a probability of 0.25.

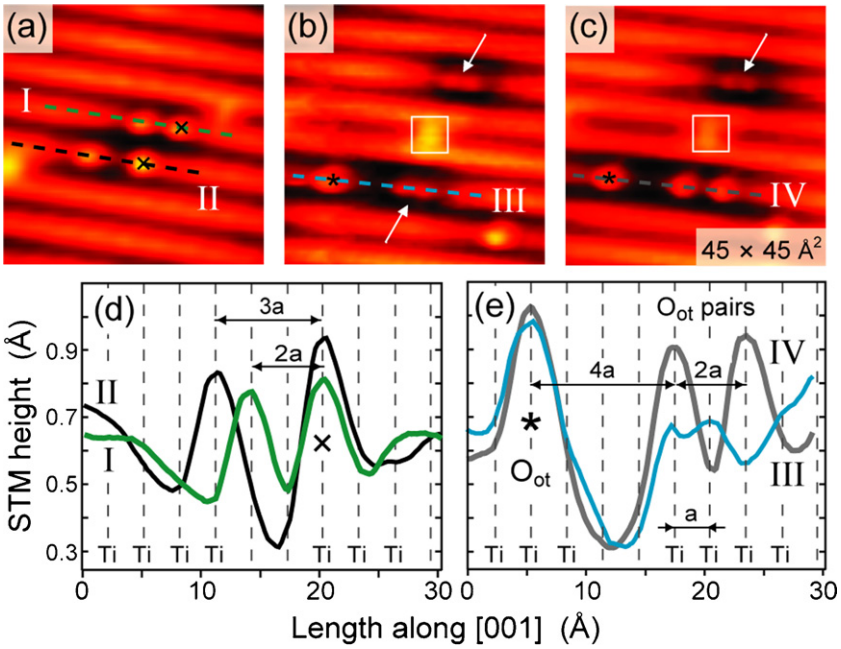

Fig. 4. (a) Zoom-in STM image obtained after 2 L O_2 exposure at RT onto low-reduced TiO_2(1 1 0). (b and c) Consecutive STM images obtained after 4 L O_2 exposure onto low-reduced TiO_2(1 1 0) at RT. Arrows indicate nearest-neighbor O_{ot} adatoms [p(1)-O_{ot} pairs] and squares denote O_{br} vacancies. (d) Line profiles along a p(2)-O_{ot} (I, black) and a p(3)-O_{ot} pair (II, green), respectively, from the STM image shown in (a). (e) Line profiles along a p(1)-O_{ot} (III, blue) and a newly formed p(2)-O_{ot} pair (IV, gray) from images (b) and (c), respectively. Positions of the 5f-Ti sites are indicated by dotted gray lines. "a" is the lattice distance in [0 0 1] direction, ~2.96 Å. (For interpretation of the references to color in this figure legend, the reader is referred to the web version of this article.)

By analyzing a series of STM images acquired on medium-high reduced TiO_2(1 1 0) crystals prior to O_2 exposure we found that configuration A does not occur [70]. This is probably due to a strong repulsion between the O_{br} vacancies along the O_{br} rows. Thus, configuration A can be ruled out as a possible starting situation for the formation of p(1)-O_{ot} pairs. On the contrary, the density of O_{br} vacancy pairs in configuration B add up to a coverage of 0.85% ML for the medium-reduced TiO_2(1 1 0) crystals and 1.8% ML for high-reduced ones. However, the density of p(1)-O_{ot} pairs (here given as the density of pairs and not as the density of O_{ot} adatoms) amounts to ~0.0% ML and ~0.6% ML for the medium- and high-reduced crystals, respectively. Assuming identical probability of the p(1)-O_{ot} pair formation starting from configuration B in both cases, the striking difference in the density of p(1)-O_{ot} pairs found for medium- and high-reduced TiO_2(1 1 0) crystals indicates that configuration B can be ruled out as a possible starting situation for the formation of p(1)-O_{ot} pairs on high-reduced crystals. Thus, since none of the O_{br} vacancy configurations sketched in Fig. 7

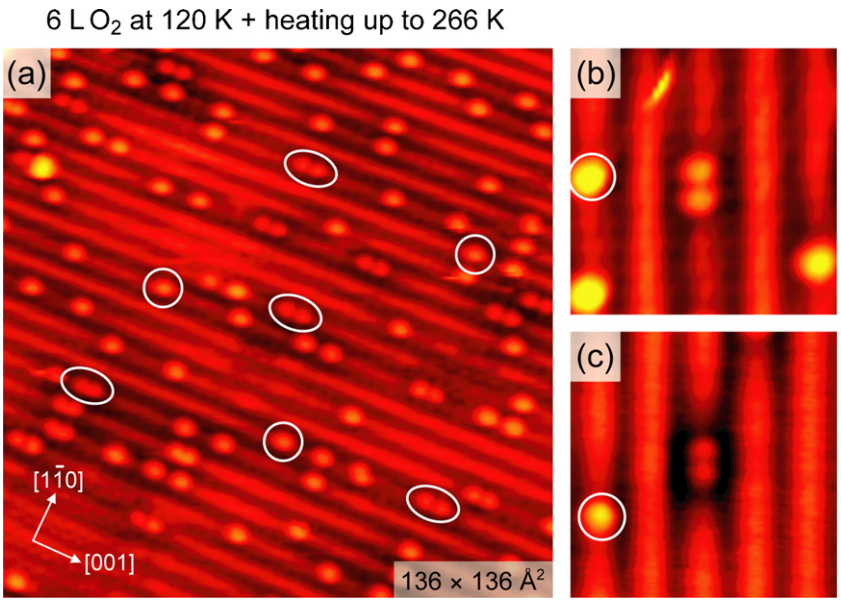

Fig. 5. (a) High-resolution STM image acquired after 6 L O_2 exposure at 120 K (accomplished via backfilling of the chamber) onto r-TiO_2(1 1 0) (~9% ML O_{br} vacancy density) followed by heating up to 266 K. White circles and ovals indicate isolated O_{ot} adatoms and p(1)-O_{ot} pairs, respectively. (b) Zoom-in STM image showing a p(1)-O_{ot} pair obtained with a special tip apex, i.e., with an adsorbate at the tip apex (same tip state as in (a)). (c) Zoom-in STM image showing a p(1)-O_{ot} pair obtained with a bare tip.

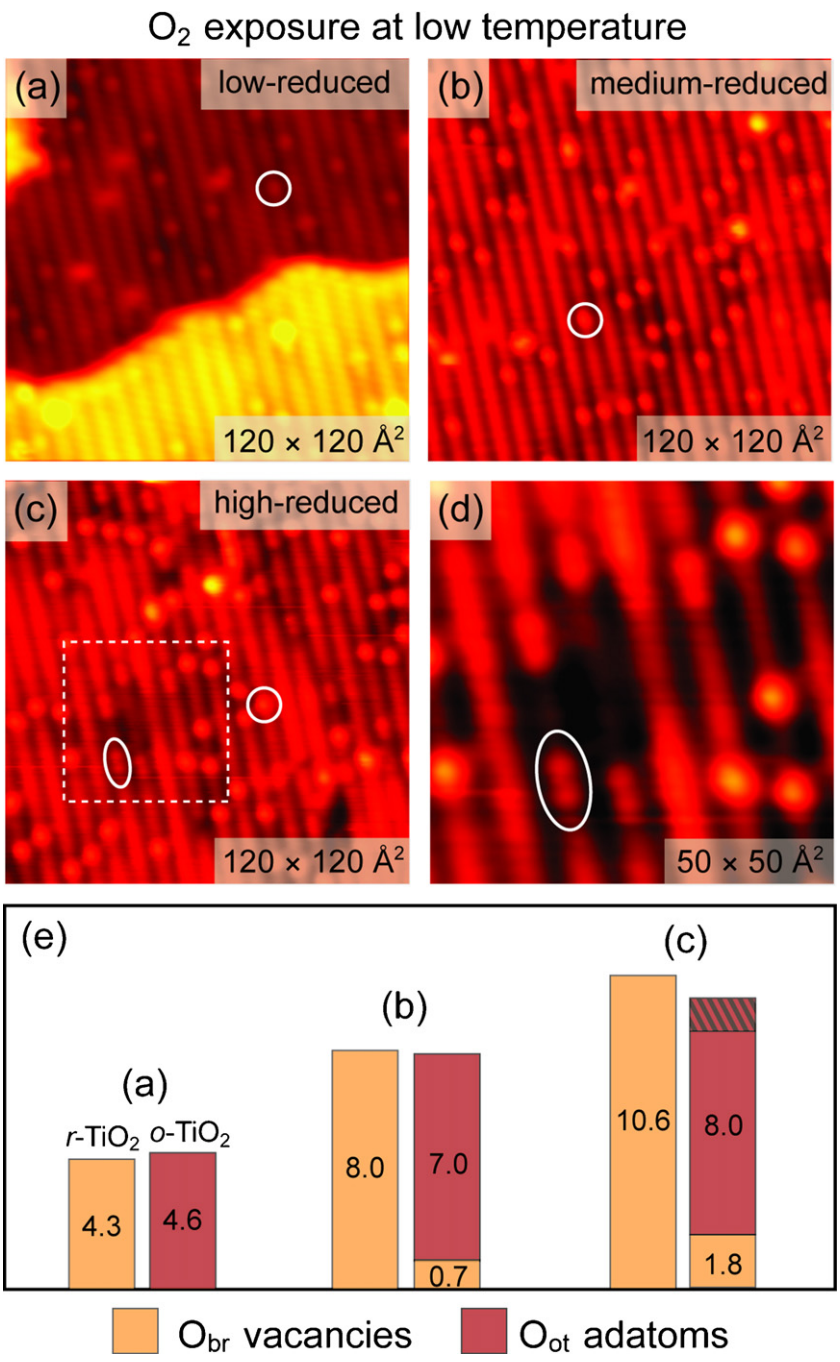

Fig. 6. STM images acquired after O_2 exposure at LT onto clean r-TiO_2(1 1 0) surfaces with O_{br} vacancy densities of ~4.3% ML (a), ~7.9% ML (b) and ~10.6% ML (c and d), respectively. O_2 exposures were 5 L (a), 10 L (b), and 50 L (c and d), respectively. The area indicated in (c) is shown enlarged in (d). Circles indicate O_{ot} adatoms and ovals p(1)-O_{ot} pairs. (e) Bar-graphs of O_{br} vacancy densities (yellow) and O_{ot} adatoms (red) in % ML before and after O_2 exposure corresponding to (a), (b) and (c and d). The hatched area represents O_{ot} adatoms occurring in p(1)-O_{ot} pairs. (For interpretation of the references to color in this figure legend, the reader is referred to the web version of this article.)

can lead to the O_{ot} adatoms found experimentally, we can rule out that the p(1)-O_{ot} pairs are created through the 1st O_2 dissociation channel. We thus conclude that on high-reduced TiO_2(1 1 0) crystals some of the O_2 molecules dissociate directly in the Ti troughs, even at 120 K. In other words, the 2nd O_2 dissociation channel is responsible for the formation of p(1)-O_{ot} pairs in spite of the low adsorption temperature. This means that the activation barrier for O_2 dissociation in the Ti troughs (2nd O_2 dissociation channel) decreases strongly with increasing reduction state of the crystal, a conclusion that is in excellent agreement with DFT calculations [13].

Fig. 8 displays the coverage of O_{ot} adatoms and O_{br} vacancies measured as a function of the reduction state, i.e., the initial O_{br} vacancy density. The density of O_{ot} adatoms increases with increasing bulk reduction, but the density of O_{br} vacancies left unfilled after the O_2 exposure increases as well. For high-reduced TiO_2(1 1 0) surfaces (initial O_{br} vacancy density ≥10% ML), it appears that $\theta_{sat}(O_{ot})$ is declining (cf. the encircled points). Based on accompanying O_2-TPD experiments we know that the O_2 exposures used in the STM studies were high enough to saturate the surface. We therefore conclude that an upper limit exists for the density of O_{ot} adatoms, $\theta_{sat}(O_{ot})$, that can be adsorbed on the o-TiO_2(1 1 0)

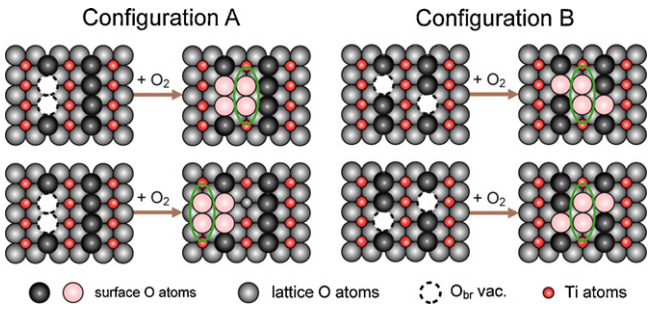

Fig. 7. Hypothetical O_{br} vacancy configurations that could lead to $p(1)$-O_{ot} pair formation at LT by dissociation of two O_2 molecules in two O_{br} vacancies in the same O_{br} row (configuration A) and in adjacent O_{br} rows (configuration B), respectively. Green ovals indicate the $p(1)$-O_{ot} pairs. (For interpretation of the references to color in this figure legend, the reader is referred to the web version of this article.)

surface. Of course, $\theta_{sat}(O_{ot})$ depends on the available charge on the surface. As further discussed below, this charge stems essentially from the near-surface region, i.e., the crystal reduction state is an essential factor that needs to be taken into consideration. Additionally, it should be considered that also O_2 molecules are adsorbed on o-TiO_2(1 1 0) surfaces [10,30,46–48], and that O_{ot} adatoms and O_2 molecules compete for the electronic charge [16,30]. Therefore, $\theta_{sat}(O_{ot})$ at LT is also influenced by coadsorbed O_2 molecules. Because the O_2 molecules are difficult to detect by means of STM [30,46–48], it remains to be resolved what the maximum total coverage of oxygen species, $\theta_{sat}(\text{oxygen}) = \theta_{sat}(O_{ot}) + \theta_{sat}(O_2)$, is on o-TiO_2(1 1 0) surfaces. Note that the existing low-temperature STM studies (temperature < 100 K) wherein STM images showing O_2 molecules on TiO_2(1 1 0) have been presented [46–48] do not cover the case of oxygen saturation.

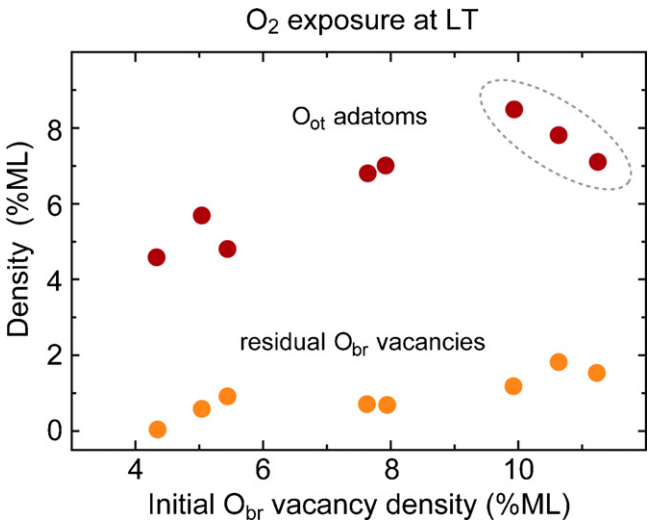

Fig. 8. Densities of O_{ot} adatoms and residual O_{br} vacancies on o-TiO_2(1 1 0) surfaces as a function of the crystal reduction state, i.e., the initial O_{br} vacancy density.

3.4. *Effect of the reduction state on the dissociative adsorption of O_2 at room temperature*

Fig. 9 displays STM results for three differently reduced TiO_2(1 1 0) crystals obtained after O_2 exposure at RT. Before oxidation the three crystals were characterized by O_{br} vacancy densities of ~4.9% ML (low-reduced), ~8.0% ML (medium-reduced) and ~9.5% ML (high-reduced), respectively. After oxidation at RT we found O_{ot} adatom densities of ~6.7% ML, ~10.2% ML, and ~11.3%

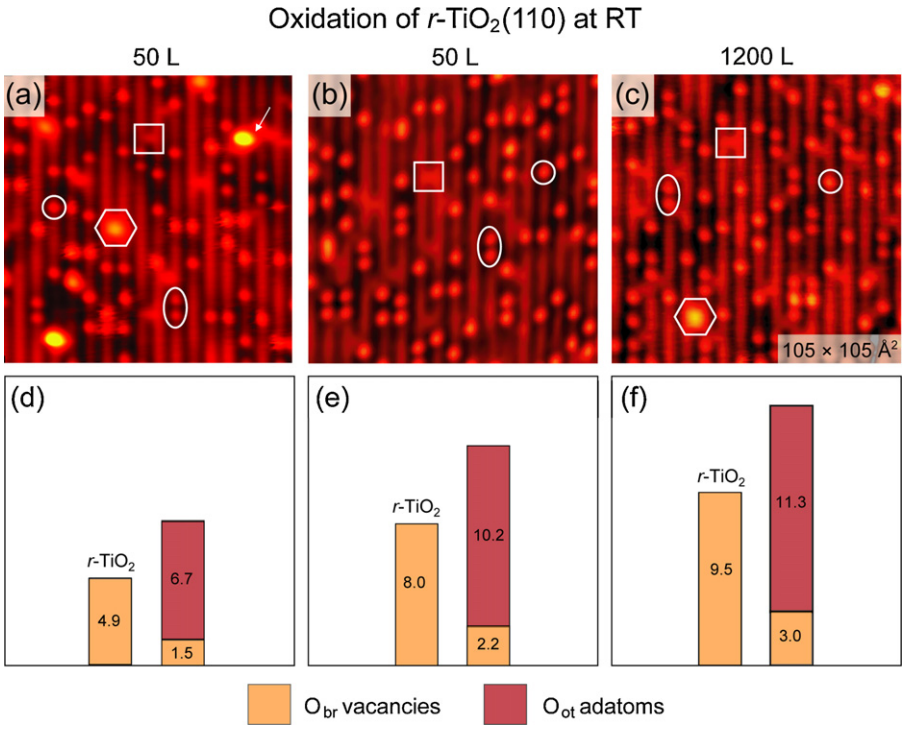

Fig. 9. (a)–(c) STM images obtained after O_2 exposure at RT onto differently reduced TiO_2(1 1 0) crystals. O_2 exposures in three separate experiments were 50 L (a and b), and 1250 L (c), respectively. Squares indicate O_{br} vacancies, circles O_{ot} adatoms, ovals $p(2)$-O_{ot} pairs and hexagons paired H adatoms. The arrow in (a) indicates a water monomer. (d)–(f) Bar-graphs of estimated coverage of O_{br} vacancies (yellow) and O_{ot} adatoms (red) in %ML before and after O_2 exposure in the three experiments compared. Bar-graphs in (d) correspond to (a), (e) to (b) and (f) to (c), respectively. (For interpretation of the references to color in this figure legend, the reader is referred to the web version of this article.)

ML, respectively (Fig. 9d–f). Because the O_{ot} adatom densities exceed the corresponding densities of O_{br} vacancies before the oxidation one may expect that all the O_{br} vacancies were healed upon oxidation. However, this is not the case. Instead, ~1.48% ML, ~2.2% ML, and ~3.0% ML O_{br} vacancies, respectively, remained unfilled in spite of the high O_2 exposures and the relatively high densities of O_{ot} adatoms (Fig. 9d–f). Thus, the adsorption of oxygen species on TiO_2(1 1 0) is limited both at LT as well as at RT. However, at RT and this low pressure range the adsorption of O_2 molecules is unlikely [10,13,30,44,53] and the 2nd O_2 dissociation channel is in operation at all crystal reduction states [cf. the p(2)-O_{ot} pairs indicated by while ovals in Fig. 9a–c]. Because of the self-limitation of the O_2 dissociation reaction due to charge depletion, and because O_{br} vacancies are not filled via the 2nd O_2 dissociation channel, more O_{br} vacancies remain unfilled at RT compared to the situation when r-TiO_2(1 1 0) surfaces are exposed to O_2 at LT.

3.5. Annealing of o-TiO_2(1 1 0) surfaces

We now turn to the discussion of STM results obtained after thermal activation of oxygen and Ti species on o-TiO_2(1 1 0). Starting points in the described experiments were differently reduced TiO_2(1 1 0) crystals with initial O_{br} vacancy densities ranging from ~2 to ~10% ML. Throughout, O_2 was dosed at LT. Subsequently, the o-TiO_2(1 1 0) surfaces were annealed at 393 K for 120 s. Following this preparation recipe, we obtained TiO_2(1 1 0) surfaces with O_{ot} adatoms and small TiO_x islands (Fig. 10). In Fig. 10a–d some of the O_{ot} adatoms are marked by circles, whereas some of the TiO_x islands are indicated by hexagons. In agreement with previous studies [13,30,45], the prevailing TiO_x islands are characterized by an apparent STM height of ~2.2 Å. Because no sign of reduction was observed in valence band spectroscopic measurements after annealing at 393 K [13], most of the TiO_x islands on the surfaces are stoichiometric. The TiO_x islands are the result of Ti interstitial diffusion towards the surface where they react with O_{ot} adatoms and possibly also with O_2 molecules [13,30,45].

For low-reduced TiO_2(1 1 0) surfaces (Fig. 10a and b) only very few TiO_x islands appeared after annealing at 393 K, whereas a higher density of TiO_x islands appeared on medium- and high-reduced TiO_2(1 1 0) crystals (Fig. 10c and d). On the contrary, the density of O_{ot} adatoms was found to be very high on low-reduced TiO_2(1 1 0) surfaces, whereas low densities of O_{ot} adatoms were evident on medium- and high-reduced TiO_2(1 1 0) crystals (Fig. 10e). Fig. 10e shows the ratio, R, between the O_{ot} adatom density (obtained after O_2 exposure at LT and annealing at 393 K) and the initial O_{br} vacancy density as function of the crystal reduction state:

$$R = \frac{O_{ot}\text{ adatom density after }O_2\text{ exposure at LT followed by annealing at 393 K for 120 s}}{\text{initial }O_{br}\text{ vacancy density}}$$

For low-reduced TiO_2(1 1 0) crystals we found $R > 2$, which underlines the occurrence of the 2nd O_2 dissociation channel. However, between 5 and 6% ML O_{br} vacancy density R declines strongly, and R is even smaller than one for O_{br} vacancy densities >6.5% ML. The latter is a result of the low O_{ot} densities found for medium- and high-reduced TiO_2(1 1 0) crystals after brief annealing at 393 K. Because the declining density of O_{ot} adatoms with higher crystal reduction state is accompanied by an increasing density of TiO_x islands (cf. Fig. 10f), we infer that the decline of R with increasing reduction state is caused by enhanced Ti interstitials diffusing towards the surface. The more Ti interstitials react with oxygen species, O_{ot} adatoms and O_2 molecules, respectively, the more TiO_x islands are formed on the surface and the lower is the density of O_{ot} adatoms.

We performed two additional annealing experiments with TiO_2(1 1 0) crystals of different reduction states (Fig. 11). In these

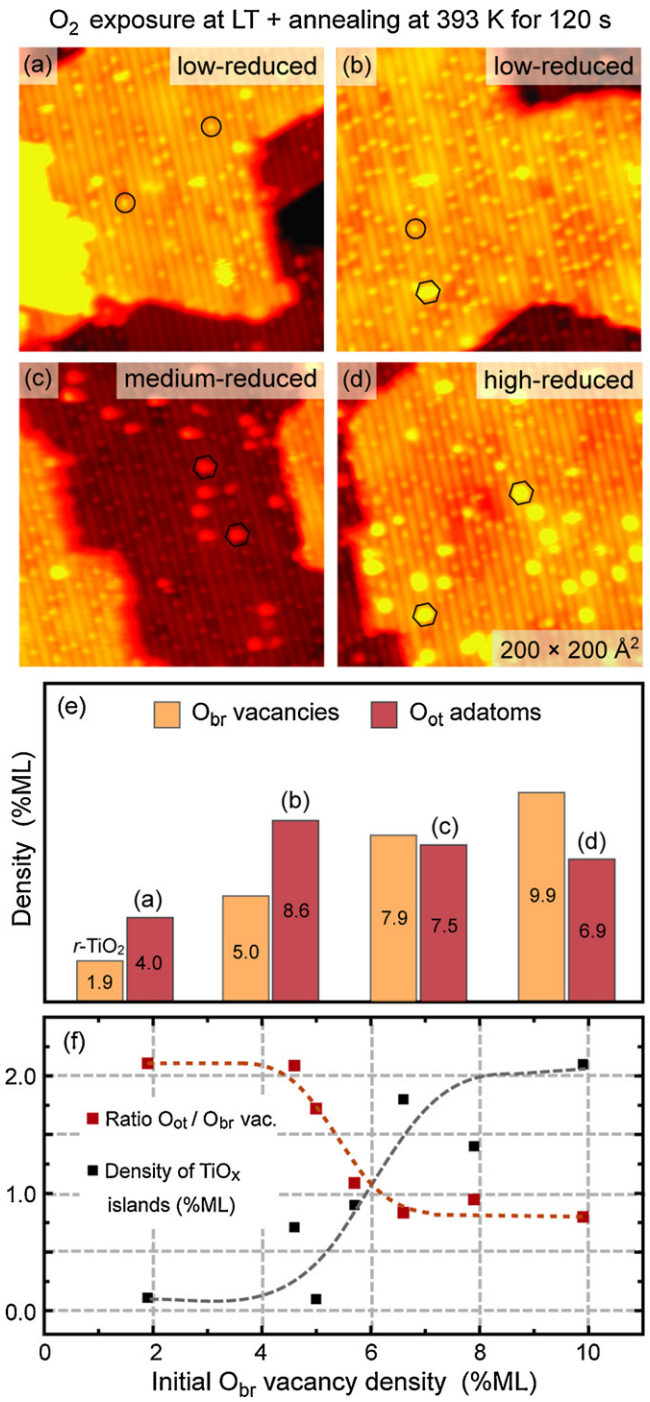

Fig. 10. (a)–(d) STM images acquired on differently reduced TiO_2(1 1 0) crystals after 20 L O_2 exposure at 130 K and subsequent annealing at 393 K for 120 s. Low-reduced TiO_2(1 1 0) (a and b), medium-reduced TiO_2(1 1 0) (c) and high-reduced TiO_2(1 1 0) (d), respectively. (e) Density of O_{br} vacancies (yellow) and O_{ot} adatoms (red) in %ML before and after O_2 exposure and annealing corresponding to (a), (b), (c) and (d), respectively. (f) Ratio, R, of O_{ot} adatoms after O_2 exposure followed by annealing at 393 K and O_{br} vacancies before the exposure (red squares). The density of TiO_x islands after annealing at 393 K is also shown (black squares). (For interpretation of the references to color in this figure legend, the reader is referred to the web version of this article.)

experiments the TiO_2(1 1 0) surfaces were exposed to O_2 at LT as in the experiments summarized in Fig. 10. However, after the O_2 exposure at LT we annealed the samples for 120 s at much higher temperature, 623 K, to ensure that the maximum possible coverage of TiO_x islands has indeed been achieved. In the first experiment we

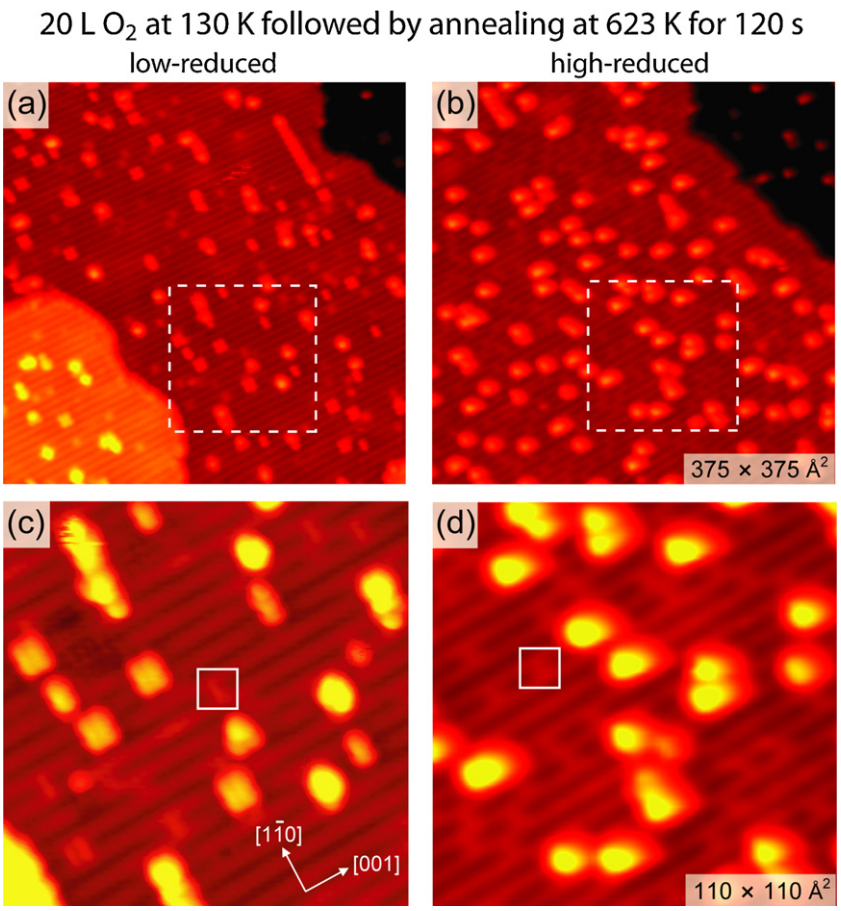

Fig. 11. STM images acquired on differently reduced TiO_2(1 1 0) crystals after 20 L O_2 exposure at 130 K (accomplished via backfilling of the chamber) and subsequently annealing at 623 K for 120 s: (a) Low-reduced TiO_2(1 1 0) crystal characterized by ~3.5% ML O_{br} vacancies and (b) high-reduced TiO_2(1 1 0) crystal (~10% ML O_{br} vacancies). Areas indicated in (a) and (b) are shown enlarged in (c) and (d), respectively. Squares in (c) and (d) label O_{br} vacancies.

studied a low-reduced TiO_2(1 1 0) crystal (O_{br} vacancy density of ~3.5% ML). After a 20 L O_2 exposure at 133 K and annealing to 623 K, we observed quite small TiO_x islands on the surface of this crystal, as shown in Fig. 11a and c. The height of the obtained TiO_x islands is, in average, ~3 Å, and the length in [0 0 1] direction ~8 Å. The second experiment of this type was performed on a high-reduced TiO_2(1 1 0) crystal (O_{br} vacancy density ~10% ML), cf. Fig. 11b and d. Clearly, the TiO_x islands formed on the surface of this crystal are larger than that found on the low-reduced TiO_2(1 1 0) crystal. The apparent STM height of the TiO_x islands on the high-reduced TiO_2(1 1 0) crystal is, in average, ~4 Å, and the length of the TiO_x islands is ~12 Å. These results confirm that more oxygen species react with high-reduced TiO_2(1 1 0) crystals, forming larger TiO_x islands on the surface, than on low-reduced TiO_2(1 1 0) crystals. The results presented in Figs. 10 and 11 are in excellent agreement with previous data reported by Li et al. [39,40]. In Ref. [39] it has been reported that the adstructures obtained after annealing in oxygen depend very much on the sample history, i.e., on the reduction state of the TiO_2(1 1 0) crystal.

3.6. *Effect of the reduction state on the O_2 desorption between ~360 K and ~450 K*

Fig. 12 summarizes O_2-TPD spectra all obtained from the same sample, but with the TiO_2(1 1 0) crystal in different reduction states. In its low- and medium-reduced state (Fig. 12a), the maximum O_2 desorption occurred at ~410 K (β-peak), and a shoulder was evident at ~386 K (α-peak). However, when the TiO_2(1 1 0) crystal was high-reduced (Fig. 12b), the α-peak was more intense than the β-peak. Considering the STM data presented above, this change of the line shape of the O_2-TPD spectra between low/medium- and high-reduced TiO_2(1 1 0) crystals may be rationalized. The STM data shown in Fig. 10 revealed that the formation of TiO_x islands ($x \sim 2$) begins on low- and medium-reduced TiO_2(1 1 0) crystals at slightly higher temperature than on high-reduced crystals. Concomitantly, the maximum O_2 desorption on such crystals occurs predominantly at the high temperature, ~410 K. On the contrary, on high-reduced TiO_2(1 1 0) crystals that are characterized by large terraces the formation of TiO_x islands occurs already at slightly lower temperatures, concomitant with the desorption of O_2 molecules predominantly in the α-peak at ~386 K, i.e., at slightly lower temperature than on low- and medium-reduced TiO_2(1 1 0) crystals. That two peaks occur in the O_2-TPD spectra could be related to the fact that the diffusion of Ti interstitials towards the surface is easier beneath central areas of the terraces than beneath surface regions in the proximity to the step edges. Interestingly, electron paramagnetic resonance (EPR) measurements by Aono and Hasiguti [71] suggested that Ti interstitials tend to cluster into pairs or even larger arrangements of Ti interstitials. It is possible that the Ti interstitial diffusion towards the surface is facilitated if they occur in such clusters. Thus, the change in the line shape of the O_2-TPD spectra between low/medium- and high-reduced TiO_2(1 1 0) crystals may be rationalized invoking an enhanced occurrence of Ti interstitials in clusters for high-reduced TiO_2(1 1 0) crystals. However, because the number of possible defect configurations in the bulk is very large, our interpretation of the double-peak structure in the O_2-TPD spectra remains somewhat speculative.

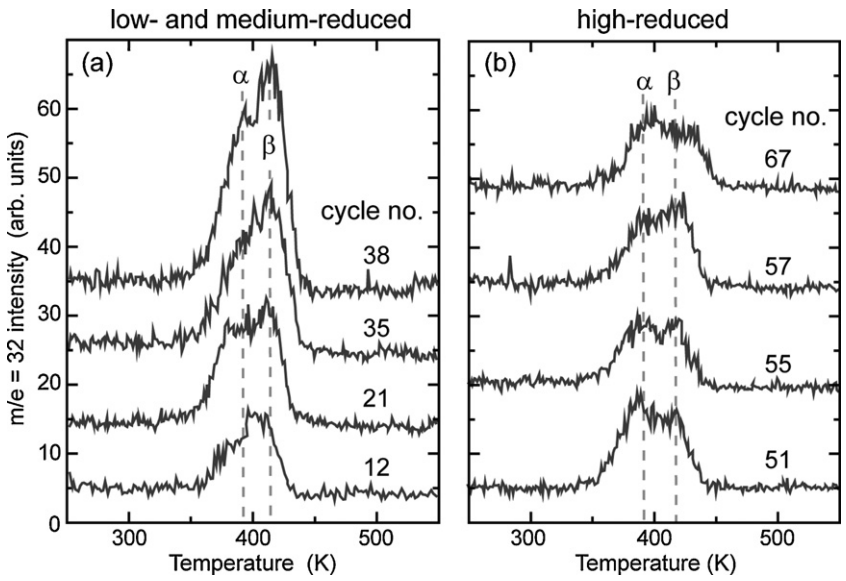

Fig. 12. O_2-TPD spectra obtained on low- and medium-reduced TiO_2(1 1 0) crystals (a) and high-reduced TiO_2(1 1 0) crystals (b), respectively. O_2 (≥20 L) was throughout dosed at 130 K, and the heating rate was 2 K/s. Applied numbers of preparation cycles are given directly in the plots.

Fig. 13a shows the integrated O_2-TPD peak area as a function of the crystal reduction state that is given here as the number of applied preparation cycles, each consisting of Ar^+ sputtering followed by vacuum-annealing. For a more complete description of the sample preparation we additionally show the chosen annealing temperatures (Fig. 13b). Furthermore, Fig. 13 shows the obtained terrace width (Fig. 13c), the O_{br} vacancy density (Fig. 13d) and the integrated area of the Ti 3d defect state (Fig. 13e) as function of the applied preparation cycles. With the exception of the Ti 3d defect state areas, which are a direct measure of the Ti^{3+} excess charge, all the data displayed in Fig. 13 were acquired using the same TiO_2(1 1 0) crystal. The Ti 3d defect state measurements were obtained on a different crystal that was prepared following similar preparation procedures. The reduction state of rutile TiO_2(1 1 0) crystals prepared under UHV conditions was found to depend both on the number of preparation cycles and the chosen annealing temperature. During the first 10 preparation cycles the temperature of ~823 K during annealing was kept constant until it was possible to acquire STM images of high quality. Upon further reduction of the crystal we increased the annealing temperature in steps of 10 K on average after each 5 cycles in order to obtain/maintain TiO_2(1 1 0) surfaces with large terraces width. Upon sample reduction, both the O_{br} vacancy density (Fig. 13d) as well as the integrated area of the Ti 3d defect state (Fig. 13e) increase. Thus, a correlation exists between surface reduction (probed by STM) and the reduction of the near-surface region (probed by valence band PES). In retrospective, these results justify the use of the O_{br} vacancy density as a measure of the bulk reduction state (see above). It should be noted, however, that much care must be taken to interpret the correlation between the integrated area of the Ti 3d defect state and the O_{br} vacancy density correctly [13,72]. More specifically, alone from the fact that a correlation seems to exists between the Ti 3d defect state and the O_{br} vacancy density does not allow one to deduce what the origin of the Ti 3d defect state is. The results displayed in Fig. 13d and e are not surprising because we simultaneously altered the bulk- and surface reduction state.

In the O_2-TPD experiments corresponding to the O_2-TPD peak areas plotted in Fig. 13a we used both *r*- and *h*-TiO_2(1 1 0) surfaces, and in either case the surface was saturated with O_2 at ~130 K. The O_2-TPD peak areas can be compared for *r*- and *h*-TiO_2(1 1 0) surfaces, because equal amounts of O_2 desorb from the surface provided that the bulk-reduction, the surface morphology and the adsorption temperatures are comparable (cf. Fig. 2). During the first 40 preparation cycles the amount of O_2 that desorbs between ~360 K and at ~450 K increases, and a maximum is observed for the 40th cycle. Upon further reduction of the crystal, the amount of desorbing O_2 declines. This is a remarkable result that cannot be explained within O_2 adsorption models wherein surface defects, O_{br} vacancies and H_{ad} species, respectively, are proposed as the main charge donors, enabling O_2 adsorption on the surface. If the O_2 molecules were adsorbed on the surface essentially through charge transfer from surface defects the amount of desorbing O_2 should scale directly with the density of O_{br} vacancies and H_{ad} species. However, the decline of the O_2-TPD peak area for crystal reduction states obtained after the application of more than 40 preparation cycles can be understood when O_2 adsorption on reduced TiO_2(1 1 0) crystals is enabled through charge transfer from defects in the near-surface region [49].

On low-reduced TiO_2(1 1 0) crystals only a small amount of O_2 adsorbs, i.e., the amount of desorbing O_2 at ~410 K is limited by the O_2 adsorption at 130 K. With increasing bulk-reduction of the crystal more Ti^{3+} excess charge is available on the TiO_2(1 1 0) surface, and thus more O_2 adsorbs. As a result, the O_2-TPD peak at ~410 K increases initially, i.e., during the first 40 preparation cycles. We know, however, that the O_2 molecules desorbing between ~360 K and at ~450 K constitute only a fraction of the O_2 molecules adsorbed at LT. One part of the adsorbed O_2 molecules desorbs between ~130 K and ~360 K, i.e., directly after starting of the temperature ramp [10,11,30,59], and another part is lost due to O_2 dissociation (2nd channel) followed by TiO_x island formation. Therefore, the amount of desorbing O_2 between ~360 K and at ~450 K is determined by two variables, the quantity of adsorbed O_2 (at 130 K) and the quantity of the O_2 loss upon temperature increase in the TPD experiment. When the crystal reduction exceeds a certain degree, the O_2 loss upon heating becomes so high that the residual amount of intact O_2 molecules desorbing at ~410 K is smaller than on *o*-TiO_2(1 1 0) surfaces with the crystal being only at medium-reduced. This, to a large extent, explains the occurrence of a maximum in the O_2-TPD peak area at intermediate reduction states.

The utilized experimental techniques did not allow us to quantify $\theta_{sat}(O_2)$ after O_2 adsorption at 130 K. Nevertheless, because the

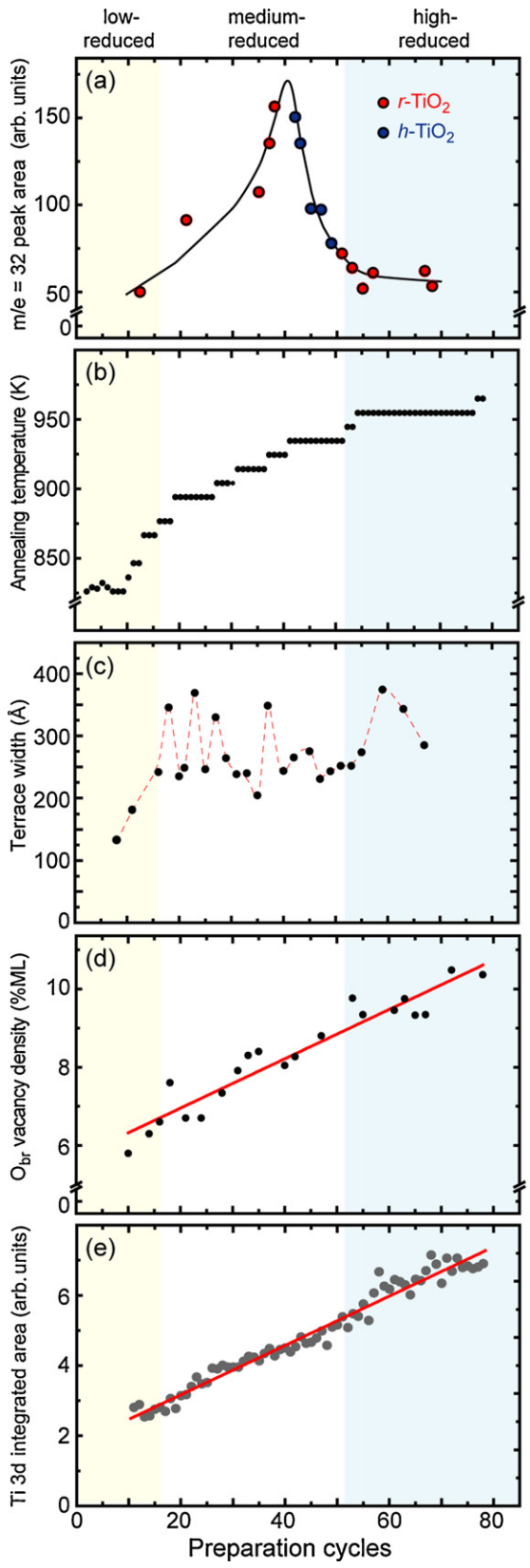

Fig. 13. O_2-TPD integrated area (a), annealing temperature (b), terrace width (c), O_{br} vacancy density (d) and integrated Ti 3d peak area (e) as a function of preparation cycles, each cycle consisting of sputtering and vacuum-annealing. Red and blue dots represent integrated O_2-TPD areas obtained for *r*-TiO_2 and *h*-TiO_2 surfaces, respectively. The terrace width was deduced from STM images of 800² Å² size. The Ti 3d defect states were measured on another crystal. (For interpretation of the references to color in this figure legend, the reader is referred to the web version of this article.)

Ti^{3+} excess charge increases upon sample reduction (Fig. 13e), it is reasonable to assume that $\theta_{sat}(O_2)$ scales with the crystal reduction state. However, for high-reduced TiO_2(1 1 0) crystals $\theta_{sat}(O_2)$ is probably sufficiently high so that the Coulombic repulsion between the O_2 molecules becomes an important factor that inhibits a further increase of $\theta_{sat}(O_2)$. The relatively small values for $\theta_{sat}(O_{ot})$, 6.0–8.5% ML, obtained on high-reduced TiO_2(1 1 0) crystals after O_2 adsorption at 130 K (cf. Fig. 8) are in line with this hypothesis. Even though the 2nd O_2 dissociation channel occurs on high-reduced TiO_2(1 1 0) crystals at 120 K (cf. Fig. 6) no further increase of $\theta_{sat}(O_{ot})$ was observed. Rather, the STM data summarized in Fig. 8 indicate that $\theta_{sat}(O_{ot})$ is declining for O_{br} vacancy densities >10% ML (see the three data points within the dotted oval). This result is consistent with competition for the excess charge that is expected for large $\theta_{sat}(O_2)$.

Assuming that $\theta_{sat}(O_2)$ has reached a maximum after ~40 preparation cycles, it is conceivable that the O_2-TPD peak area declines, as observed experimentally (Fig. 13a). The fact that more oxygen species react with high-reduced TiO_2(1 1 0) crystals upon heating of the sample than on low- and medium-reduced ones as observed by STM (cf. Figs. 10 and 11) supports our conclusion that the decline of the O_2-TPD peak area upon further reduction of the crystal after 40 preparation cycles is related to the loss of O_2 molecules before O_2 desorption sets in. Because of the higher amount of the available excess charge this loss of O_2 molecules is higher on high-reduced crystals than on low- and medium reduced ones. The more Ti^{3+} excess charge is available on the TiO_2(1 1 0) surface the easier are the processes that lead to the formation of the TiO_x islands.

An additional possible reason for the decline of the O_2-TPD peak area after ~40 preparation cycles is that $\theta_{sat}(O_2, 130\,K)$ is smaller for high-reduced TiO_2(1 1 0) crystals than for medium-reduced ones. This hypothesis is plausible, supposed we assume a variable charge state of the O_2 molecules, depending on the crystal reduction state. For example, for a medium-reduced TiO_2(1 1 0) crystal the prevailing charge state of the O_2 molecules might be −1, corresponding to superoxide O_2 ions, as has been suggested previously [10]. In this case, the Coulombic repulsion between the O_2 molecules is moderate, resulting in O_2 coverage at 130 K on *o*-TiO_2(1 1 0) of up to 40% ML [30]. On the contrary, on high-reduced TiO_2(1 1 0) crystals more excess charge is available, cf. Fig. 13e. This may lead to a situation where the prevailing charge state of the chemisorbed O_2 molecules is −2, corresponding to peroxo O_2 ions. In this case the Coulombic repulsion between the O_2 molecules is substantial, leading to O_2 saturation coverage that are smaller than on medium-reduced TiO_2(1 1 0) crystals. Indeed, recent ultraviolet PSD experiments by Petrik and Kimmel suggest that the charge state of O_2 molecules is variable [16], rendering the charge state of the chemisorbed O_2 molecules an important factor that needs to be considered. The STM and TPD data presented here are consistent with a variable charge state of the chemisorbed O_2 molecules, depending on the crystal reduction state. We consider the results summarized in Fig. 13 as strong indication for charge transfer from the near-surface region to chemisorbed oxygen species.

3.7. *Relevance to applications in catalysis and photocatalysis*

The presented study has implications to heterogeneous catalysis since TiO_2 is a widely used support for metal catalysts, and the electronic state of the TiO_2 support will certainly influence the catalytic properties of the metal/oxide composite catalyst [38]. The new insight gained here is also useful in photochemistry where TiO_2 is electronically excited, for example by sunlight. Depending of the available Ti^{3+} excess charge the nature of the prevailing chemisorbed oxygen species may change. This knowledge is particularly interesting for applications of TiO_2-based materials as

photo-oxidation catalysts. Today, mechanistic insight into photochemical processes is still scarce, and it is not clear yet which oxygen species is the main player in photoreactions [8,9].

The presented data help to better link model studies performed under UHV conditions with more applied studies in the field of materials science. For example, the understanding of why O_2 molecules can be stabilized on bulk-reduced TiO_2(1 1 0) crystals and desorb at unusual high temperatures offers a straightforward explanation of how O_2 molecules can be stabilized on the surfaces of catalysts and photo-catalysts even in the absence of surface O vacancies: The O_2 molecules are simply stabilized through charge transfer from the near-surface region (ionosorption model). In this regard it is noteworthy that striking similarities exist between O_2-TPD spectra obtained on rutile powder samples [73,74] with those measured on well-characterized rutile TiO_2(1 1 0) crystals. It is also noteworthy that unexpected adsorption/desorption of O_2 has been revealed for TiO_2 nanotube arrays [75], and further that even under ambient pressure a narrow O_2 desorption peak at ~400 K has been identified in TPD spectra on H_2O_2 treated "real" TiO_2 photocatalysts [76]. In all these studies [70–73], it is unlikely that surface O vacancies persisted at the applied high-pressure conditions.

In this light, the presented data are further indication that surface O vacancies are of only minor relevance for "real" catalysts and photo-catalysts [32]. Because temperatures higher than 500 K are required for their creation [50,77], surface O vacancies are very unlikely to play a role for reaction running at temperatures lower than 500 K. Alone the fact that it is rather difficult to produce TiO_2(1 1 0) surfaces with clean O_{br} vacancies [*r*-TiO_2(1 1 0)] even under UHV [34,41,78] points to the view that surface O vacancies are of only minor relevance in the applications of TiO_2. On the contrary, bulk-defects can easily persist under the high-pressure conditions at which catalyzed reactions and photo-reaction are running, and therefore we consider the presence of charge donating bulk-defects in the near-surface region as much more plausible explanation of how oxygen species can be stabilized at the surfaces of catalysts and photo-catalysts. The data presented here may also be of relevance for an improved understanding of the surface processes occurring on other reducible oxides such as anatase TiO_2, SnO_2 and ZnO.

4. Conclusions

Using high-resolution STM and sample ensemble averaging techniques such as TPD and PES we found that the interaction of O_2 with TiO_2(1 1 0)–(1 × 1) depends strongly on the crystal reduction state. TiO_2(1 1 0) crystals are classified as low-, medium- and high-reduced for O_{br} vacancy densities of 2–6% ML, 6–9% ML, and 9–12% ML, respectively. Specifically, we found that

i) the energy barrier for the 2nd, non-vacancy-assisted O_2 dissociation channel decreases with increasing reduction state. On low-and medium-reduced TiO_2(1 1 0) crystals the 2nd O_2 dissociation channel sets in between 150 K and 180 K [30]. However, on high-reduced TiO_2(1 1 0) crystals the 2nd O_2 dissociation channel sets in at temperatures as low as 120 K.
ii) an upper limit exists for the density of O_{ot} adatoms that can be stabilized on clean, high-reduced TiO_2(1 1 0)–(1 × 1). At 130 K, this limit is close to 8% ML, whereas ~11% ML O_{ot} adatoms can be stabilized after high O_2 exposure at RT. Some O_{br} vacancies are left unfilled on TiO_2(1 1 0) surfaces because the Ti^{3+} excess charge in the near-surface region has been depleted. Because O_{br} vacancies are not filled via the 2nd O_2 dissociation channel, more O_{br} vacancies remain unfilled at RT compared to the situation when *r*-TiO_2(1 1 0) surfaces are exposed to O_2 at 110–150 K.
iii) the ratio between the O_{ot} adatoms obtained after O_2 adsorption at low temperature followed by annealing at 393 K and the initial density of O_{br} vacancies declines with increasing reduction state. Simultaneously, the density of TiO_x islands ($x \sim 2$) increases after annealing at 393 K for 120 s, indicating that Ti interstitial diffusion is slightly more facile in high-reduced TiO_2(1 1 0) crystals compared to low-reduced ones.
iv) the shape of the O_2-TPD peak occurring between ~360 K and ~450 K depends on the crystal reduction state. For high-reduced TiO_2(1 1 0) crystals with large terraces most O_2 molecules desorb at ~386 K, whereas O_2 desorption is peaking at ~410 K for low- and medium-reduced crystals. However, on *h*-TiO_2(1 1 0) surfaces the O_2 desorption is peaking at ~410 K regardless of the crystal reduction state. This observation is probably linked to a more homogeneous distribution of the Ti^{3+} excess charge in the near-surface region of *h*-TiO_2(1 1 0) compared to the situation faced on *r*-TiO_2(1 1 0) surfaces. On *r*-TiO_2(1 1 0) surfaces, the two peaks in the O_2-TPD spectra may occur because the Ti interstitial diffusion towards the surface is easier beneath central areas of the terraces than beneath surface regions in the proximity to the step edges.
v) the quantity of O_2 desorbing between ~360 K and ~450 K reaches a maximum at intermediate crystal reduction states. For high-reduced TiO_2(1 1 0) crystals, more O_2 is lost upon temperature increase, leading to a decline of the O_2-TPD peak area. That more oxygen is incorporated into the near-surface region can be rationalized by a lowered O_2 dissociation barrier (2nd channel), the Ti interstitial density and the ease of Ti interstitial diffusion in high-reduced crystals. As a consequence, the TiO_x islands ($x \sim 2$) found on high-reduced TiO_2(1 1 0) crystals are larger than those found on low- and medium-reduced crystals. An additional factor that may contribute to the decline of the O_2-TPD peak area is the O_2 saturation coverage at 130 K. For high-reduced TiO_2(1 1 0) crystals, the O_2 saturation coverage at 130 K might be smaller than that on medium-reduced TiO_2(1 1 0) crystals. This hypothesis is plausible, supposed that the prevailing charge state of the chemisorbed O_2 molecules is different, depending on the crystal reduction state.

The presented data confirm that the Ti^{3+} excess charge enabling oxygen adsorption on the rutile TiO_2(1 1 0) surface stems predominantly from sub-surface defects such as Ti interstitials [13,30] and that this charge can be easily transferred to the adsorbates, even at 130 K. Based on our comprehensive studies presented here and earlier [30,49] we find that this important conclusion is now well-documented. Surface defects such as O_{br} vacancies and H_{ad} species (OH_{br} groups) alone cannot account for all the phenomena observed for differently reduced TiO_2(1 1 0) crystals.

Acknowledgements

We gratefully acknowledge the financial support of iNANO by the Danish Research Agency, the Strategic Research Council, the Villum Kahn Rasmussen Foundation, the Carlsberg Foundation, and the European Research Council through an Advanced ERC grant (F. B.). We are grateful to Lindsay R. Merte, Bjørk Hammer and John T. Yates Jr. for stimulating discussions.

References

[1] M.A. Fox, M.T. Dulay, Chem. Rev. 93 (1993) 341–357.
[2] A. Mills, R.H. Davies, D. Worsley, Chem. Soc. Rev. 22 (1993) 417–425.
[3] M. Grätzel, Nature 414 (2001) 338–344.
[4] U. Diebold, Surf. Sci. Rep. 48 (2003) 53–229.
[5] O. Carp, C.L. Huisman, A. Reller, Prog. Solid State Chem. 32 (2004) 33–177.
[6] M. Anpo, Bull. Chem. Soc. Jpn. 77 (2004) 1427–1442.
[7] T.L. Thompson, J.T. Yates Jr., Chem. Rev. 106 (2006) 4428–4453.

[8] A. Fujishima, X.T. Zhang, D.A. Tryk, Surf. Sci. Rep. 63 (2008) 515–582.
[9] M.A. Henderson, Surf. Sci. Rep. 66 (2011) 185–297.
[10] M.A. Henderson, W.S. Epling, C.L. Perkins, C.H.F. Peden, U. Diebold, J. Phys. Chem. B 103 (1999) 5328–5337.
[11] T.L. Thompson, J.T. Yates Jr., Top. Catal. 35 (2005) 197–210.
[12] L.M. Liu, B. McAllister, H.Q. Ye, P. Hu, J. Am. Chem. Soc. 128 (2006) 4017–4022.
[13] S. Wendt, et al., Science 320 (2008) 1755–1759.
[14] A.C. Papageorgiou, N.S. Beglitis, C.L. Pang, G. Teobaldi, G. Cabailh, Q. Chen, A.J. Fisher, W.A. Hofer, G. Thornton, Proc. Natl. Acad. Sci. U.S.A. 107 (2010) 2391–2396.
[15] N.A. Deskins, R. Rousseau, M. Dupuis, J. Phys. Chem. C 114 (2010) 5891–5897.
[16] N.G. Petrik, G.A. Kimmel, J. Phys. Chem. C 115 (2011) 152–164.
[17] Z. Dohnálek, I. Lyubinetsky, R. Rousseau, Prog. Surf. Sci. 85 (2010) 161–205.
[18] U. Martinez, B. Hammer, J. Chem. Phys. 134 (2011) 194703.
[19] M.D. Rasmussen, L.M. Molina, B. Hammer, J. Chem. Phys. 120 (2004) 988–997.
[20] E. Cho, S. Han, H.S. Ahn, K.R. Lee, S.K. Kim, C.S. Hwang, Phys. Rev. B 73 (2006) 193202.
[21] C. Di Valentin, G. Pacchioni, A. Selloni, J. Phys. Chem. C 113 (2009) 20543–20552.
[22] P.M. Kowalski, M.F. Camellone, N.N. Nair, B. Meyer, D. Marx, Phys. Rev. Lett. 105 (2010) 146405.
[23] J. Stausholm-Møller, H.H. Kristoffersen, B. Hinnemann, G.K.H. Madsen, B. Hammer, J. Chem. Phys. 133 (2010) 144708.
[24] S. Chretien, H. Metiu, J. Phys. Chem. C 115 (2011) 4696–4705.
[25] V.E. Henrich, P. Cox, The Surface Science of Metal Oxides, Cambridge University Press, Cambridge, 1996.
[26] R.L. Kurtz, R. Stockbauer, T.E. Madey, E. Román, J.L. de Segovia, Surf. Sci. 218 (1989) 178–200.
[27] S. Krischok, J. Günster, D.W. Goodman, O. Höfft, V. Kempter, Surf. Interface Anal. 37 (2005) 77–82.
[28] A.G. Thomas, et al., Phys. Rev. B 75 (2007) 035105.
[29] T. Minato, et al., J. Chem. Phys. 130 (2009) 124502.
[30] E. Lira, J.Ø. Hansen, P. Huo, R. Bechstein, P. Galliker, E. Lægsgaard, B. Hammer, S. Wendt, F. Besenbacher, Surf. Sci. 604 (2010) 1945–1960.
[31] N.G. Petrik, Z.R. Zhang, Y.G. Du, Z. Dohnálek, I. Lyubinetsky, G.A. Kimmel, J. Phys. Chem. C 113 (2009) 12407–12411.
[32] S. Wendt, R.T. Vang, F. Besenbacher, in: L. Vaysieres (Ed.), On Solar Hydrogen & Nanotechnology, Wiley, New York, 2009, 467 p.
[33] G. Ertl, Angew. Chem. Int. Ed. 47 (2008) 3524–3535.
[34] C.L. Pang, R. Lindsay, G. Thornton, Chem. Soc. Rev. 37 (2008) 2328–2353.
[35] M. Bowker, R.A. Bennett, J. Phys. Condes. Matter 21 (2009) 474224.
[36] M.A. Henderson, Surf. Sci. 419 (1999) 174–187.
[37] Y.B. He, O. Dulub, H.Z. Cheng, A. Selloni, U. Diebold, Phys. Rev. Lett. 102 (2009) 106105.
[38] M. Valden, X. Lai, D.W. Goodman, Science 281 (1998) 1647–1650.
[39] M. Li, W. Hebenstreit, U. Diebold, A.M. Tyryshkin, M.K. Bowman, G.G. Dunham, M.A. Henderson, J. Phys. Chem. B 104 (2000) 4944–4950.
[40] M. Li, W. Hebenstreit, L. Gross, U. Diebold, M.A. Henderson, D.R. Jennison, P.A. Schultz, M.P. Sears, Surf. Sci. 437 (1999) 173–190.
[41] S. Wendt, et al., Surf. Sci. 598 (2005) 226–245.
[42] J. Matthiesen, et al., ACS Nano 3 (2009) 517–526.
[43] Z. Zhang, Y. Du, N.G. Petrik, G.A. Kimmel, I. Lyubinetsky, Z. Dohnálek, J. Phys. Chem. C 113 (2009) 1908–1916.
[44] Y.G. Du, N.A. Deskins, Z.R. Zhang, Z. Dohnalek, M. Dupuis, I. Lyubinetsky, Phys. Chem. Chem. Phys. 12 (2010) 6337–6344.
[45] Z. Zhang, J. Lee, J.T. Yates Jr., R. Bechstein, E. Lira, J.Ø. Hansen, S. Wendt, F. Besenbacher, J. Phys. Chem. C 114 (2010) 3059–3062.
[46] P. Scheiber, A. Riss, M. Schmid, P. Varga, U. Diebold, Phys. Rev. Lett. 105 (2010) 216101.
[47] Z.-T. Wang, Y.G. Du, Z. Dohnálek, I. Lyubinetsky, J. Phys. Chem. Lett. 1 (2010) 3524–3529.
[48] S. Tan, Y. Ji, Y. Zhao, A. Zhao, B. Wang, J. Yang, J.G. Hou, J. Am. Chem. Soc. 133 (2011) 2002–2009.
[49] E. Lira, S. Wendt, P.P. Huo, J.Ø. Hansen, R. Streber, S. Porsgaard, Y.Y. Wei, R. Bechstein, E. Lægsgaard, F. Besenbacher, J. Am. Chem. Soc. 133 (2011) 6529–6532.
[50] M.A. Henderson, W.S. Epling, C.H.F. Peden, C.L. Perkins, J. Phys. Chem. B 107 (2003) 534–545.
[51] Z. Dohnálek, J. Kim, O. Bondarchuk, J.M. White, B.D. Kay, J. Phys. Chem. B 110 (2006) 6229–6235.
[52] G.A. Kimmel, N.G. Petrik, Phys. Rev. Lett. 100 (2008) 196102.
[53] S. Porsgaard, P. Jiang, F. Borondics, S. Wendt, Z. Liu, H. Bluhm, F. Besenbacher, M. Salmeron, Angew. Chem. Int. Ed. 50 (2011) 2266–2269.
[54] G.Q. Lu, A. Linsebigler, J.T. Yates Jr., J. Chem. Phys. 102 (1995) 4657–4662.
[55] C.N. Rusu, J.T. Yates Jr., Langmuir 13 (1997) 4311–4316.
[56] C.L. Perkins, M.A. Henderson, J. Phys. Chem. B 105 (2001) 3856–3863.
[57] J. Lee, Z. Zhang, J.T. Yates Jr., Phys. Rev. B 79 (2009), 081408(R).
[58] Z. Zhang, J.T. Yates Jr., J. Phys. Chem. C 114 (2010) 3098–3101.
[59] D. Sporleder, D.P. Wilson, M.G. White, J. Phys. Chem. C 113 (2009) 13180–13191.
[60] J.V. Lauritsen, F. Besenbacher, Adv. Catal. 50 (2006) 97–147.
[61] E. Lægsgaard, L. Österlund, P. Thostrup, P.B. Rasmussen, I. Stensgaard, F. Besenbacher, Rev. Sci. Instrum. 72 (2001) 3537–3542.
[62] J. Matthiesen, J.Ø. Hansen, S. Wendt, E. Lira, R. Schaub, E. Lægsgaard, F. Besenbacher, B. Hammer, Phys. Rev. Lett. 102 (2009) 226101.
[63] J. Prunier, B. Domenichini, Z. Li, P.J. Møller, S. Bourgeois, Surf. Sci. 601 (2007) 1144–1152.
[64] Z.M. Zhang, S.P. Jeng, V.E. Henrich, Phys. Rev. B 43 (1991) 12004–12011.
[65] H. Onishi, Y. Iwasawa, Chem. Phys. Lett. 226 (1994) 111–114.
[66] S. Wendt, J. Matthiesen, R. Schaub, E.K. Vestergaard, E. Lægsgaard, F. Besenbacher, B. Hammer, Phys. Rev. Lett. 96 (2006) 066107.
[67] X.F. Cui, Z. Wang, S.J. Tan, B. Wang, J.L. Yang, J.G. Hou, J. Phys. Chem. C 113 (2009) 13204–13208.
[68] J.C. Woicik, E.J. Nelson, L. Kronik, M. Jain, J.R. Chelikowsky, D. Heskett, L.E. Berman, G.S. Herman, Phys. Rev. Lett. 89 (2002) 077401.
[69] T. Yan, J.L. Gong, D.W. Flaherty, C.B. Mullins, J. Phys. Chem. C 115 (2011) 2057–2065.
[70] E. Lira, Ph.D. thesis, Aarhus University, 2011.
[71] M. Aono, R.R. Hasiguti, Phys. Rev. B 48 (1993) 12406–12414.
[72] S. Wendt, R. Bechstein, S. Porsgaard, E. Lira, J.Ø. Hansen, P. Huo, Z. Li, B. Hammer, F. Besenbacher, Phys. Rev. Lett. 104 (2010) 259703.
[73] Y. Yanagisawa, Y. Ota, Surf. Sci. 254 (1991) L433–L436.
[74] D.D. Beck, J.M. White, C.T. Ratcliffe, J. Phys. Chem. 90 (1986) 3132–3136.
[75] S. Funk, B. Hokkanen, U. Burghaus, A. Ghicov, P. Schmuki, Nano Lett. 7 (2007) 1091–1094.
[76] S.A. Larson, J.L. Falconer, Appl. Catal. B: Environ. 4 (1994) 325–342.
[77] M.B. Hugenschmidt, L. Gamble, C.T. Campbell, Surf. Sci. 302 (1994) 329–340.
[78] S. Suzuki, K. Fukui, H. Onishi, Y. Iwasawa, Phys. Rev. Lett. 84 (2000) 2156–2159.